



Material and Si-based diode analyses of sputtered ZnTe thin films

H. H. Gullu¹ · O. Bayraklı Surucu¹ · M. Isik¹ · M. Terlemezoğlu^{2,3,4} · M. Parlak^{3,4}

Received: 30 March 2020 / Accepted: 25 May 2020 / Published online: 29 May 2020
© Springer Science+Business Media, LLC, part of Springer Nature 2020

Abstract

Structural, optical, and electrical properties ZnTe thin films grown by magnetron sputtering technique were studied by X-ray diffraction, atomic force microscopy, Raman spectroscopy, and electrical conductivity measurements. Structural analyses showed that ZnTe thin films grown on soda–lime glass substrates have a cubic crystalline structure. This crystalline nature of the films was also discussed in terms of Raman active modes. From atomic force microscopy images, the smooth and dense surface profile was observed. The conductivity of the film at room temperature was measured as $2.45 \times 10^{-4} (\Omega \text{ cm})^{-1}$ and the temperature dependency of conductivity showed Arrhenius behavior. The dark conductivity profile was modeled by thermionic emission mechanism and activation energies were extracted. In addition, the conductivity values indicated an increasing behavior with illumination intensity applied between 20 and 115 mW/cm². The heterojunction diode was generated by sputtering ZnTe film on n-Si wafer substrate and the rectification behavior was evaluated to determine the main diode parameters.

1 Introduction

In solid-state technology, group II–VI binary semiconducting thin films have been the point of interest due to their attractive material properties [1, 2]. From this point of view, CdS is one of the most popular chalcogenide material belonging to this group and used in photovoltaic applications due to its intrinsic n-type semiconducting behavior and direct band gap value of 2.42 eV [3]. Although there are several attempts on the solar partner of CdS to achieve low-cost and earth-abundant materials, CdTe is still popular in the solar market as a p-type absorber layer for thin film photovoltaic devices with its optimal direct band gap (1.45 eV) [4, 5]. Members of this family, such as ZnS, ZnSe, CdSe, and ZnTe, have attracted great attention in a wide

range of electronic and optoelectronic applications as light-emitting diodes, infrared detectors, electroluminescence devices, lasers, photo-catalysis, and THz emitters [6–9]. Due to their electronic and optoelectronic features, there is a continuing interest in their ternary and quaternary alloys together with doping by different transition metals [10–12]. In materials science, the possibilities and potentials of these structures have been research interests in both theoretical and experimental works [10–21]. In order to provide variety of new materials for optoelectronics, detailed analysis on interatomic forces, phase transition, transport coefficients, and electron–photon interactions have also been investigated by several theoretical works [15–21]. Among them, ZnTe is one of the most popular members of this family with its semiconducting characteristics such as 2.26 eV direct band gap value, p-type intrinsic semiconducting behavior, high mobility, and low electron affinity of ~ 3.53 eV [22–25]. It is a well-known material especially for the fabrication of optoelectronic and infrared detectors, and a major motivation to study this type of semiconductor depends on its response to the visible and infrared illumination and electrical characteristics to be adaptable as intrinsic or doped binary (ZnTe), and ternary (CdZnTe) compounds to these applications [26–28]. In literature, it has attracted more attention in the experimental works in the fields of semiconducting thin film structures where the structural, optical, and electrical properties have been reported by various research groups [4–30].

✉ H. H. Gullu
hasanhgullu@gmail.com; hasan.gullu@atilim.edu.tr

¹ Department of Electrical and Electronics Engineering, Atilim University, 06836 Ankara, Turkey

² Department of Physics, Tekirdag Namık Kemal University, 59030 Tekirdag, Turkey

³ Department of Physics, Middle East Technical University, 06800 Ankara, Turkey

⁴ Center for Solar Energy Research and Applications (GÜNAM), Middle East Technical University, 06800 Ankara, Turkey

With various deposition methods and on different substrates, ZnTe has been adapted to the applications in integrated electronic and optoelectronic devices. It is a promising material in the fabrication of light-emitting diodes, photovoltaic junctions and contact materials, X-ray imaging, and THZ detectors [31–35]. In addition, there are also several works on its nanostructures and monolayers for high-performance photodetectors and solar cells [36, 37]. However, there are very limited works on the temperature-dependent electrical characteristics together with the illumination effect [24, 29]. In the present work, ZnTe thin-film samples were deposited by magnetron sputtering system from the binary compound target in order to prepare stoichiometric structures on glass and Si wafer substrates. This technique was preferred with its advantage on control of deposition rate and atomic concentration in the deposition of thin films at low substrate temperatures for the possible large-scale applications. In order to contribute to the literature and to present complete understanding of the electrical properties of ZnTe film, temperature-dependent electrical measurements were performed on the samples deposited in van der Pauw geometry on the glass substrate and the results were discussed under the aim of possible optoelectronic applications. The dark activation energies were calculated and the photo-response of the samples were analyzed under the effect of different illumination conditions. In addition to the material characterization of the thin film on deposited glass substrate, the Si-based diode structure was fabricated in order to present the complete results in material and device characteristics. Based on current–voltage (I – V) measurements, device behavior and diode parameters of the In-dot top contacted on p-ZnTe/n-Si diode structure were investigated in dark and room temperature conditions.

2 Experimental details

In this work, ZnTe thin-film layer was deposited on chemically cleaned glass substrates and n-Si wafer by single-magnetron RF sputtering system. During the deposition, 3-inch diameter, high-purity (99.99%) ZnTe target was sputtered onto the substrate surface where the substrate temperature was kept constant at 200 °C. Before the deposition, the system was stabilized under low vacuum about 10^{-5} Pa, whereas to start the deposition process, the base pressure was adjusted to 10^{-1} Pa with a continuous pure Ar flow in the rate of 6 sccm. The deposition was performed by applying forward sputtering RF power of 75 W and deposition conditions were adapted to obtain about 2 Å/s deposition rate. The thickness of the ZnTe thin films was in-situ controlled by Inficon XTM/2 deposition/thickness monitor and after deposition, it was measured using Dek-tak 6M profilometer as about 500 nm. Energy dispersive

X-ray (EDS) works, which were carried out by Quanta 400 FEG model SEM equipped with EDAX facility, showed that the deposited thin films were in stoichiometric composition having nearly the atomic percentage of 50.0 to 50.0 of the constituent elements. The crystalline properties of the films were investigated by Rigaku Miniflex X-ray diffraction (XRD) system equipped with Cu-K α X-ray source ($\lambda = 1.54$ Å). Raman scattering spectrum recorded in the frequency range of 100–500 cm^{-1} with Horiba Yvon RMS-550 Raman spectrometer was obtained by 532 nm line of YAG:Nd3+ laser. Surface topography and roughness characterizations were performed using Veeco Multi-mode V atomic force microscopy (AFM) system in tapping mode. The optical characteristics of the films were investigated by using spectral transmission measurements in the wavelength range of 300–1000 nm with by Perkin-Elmer Lambda 45 spectrophotometer. In order to perform electrical measurements, thin films were deposited on glass substrates masked in van der Pauw geometry and after deposition, 99.99% pure In elemental source were evaporated on the ZnTe samples through suitable metal shadow mask for front ohmic contact. Then, samples were annealed at 100 °C to improve the adhesion of the metal contacts on the film surface. This process was also performed to obtain front metal contact ZnTe/Si diode. On the other hand, back contact of the diode was deposited on Si wafer by thermal evaporation of Ag-metal. A detailed energy band diagram of the diode is shown in Fig. 1. In this figure, the electron affinity of ZnTe and n-Si layers are assumed to be 3.53 and 4.05 eV, respectively [37–39]. In addition, using these values, conduction band offset (ΔE_C) is found as 0.52 eV and valence band offset (ΔE_V) is calculated as 0.62 eV. The band gap energies are also presented as 2.26 and 1.12 eV for ZnTe and n-Si, respectively [38, 40]. Temperature-dependent conductivity measurements were accomplished under a vacuum of about 10^{-3} Pa within Janis liquid nitrogen cryostat in the interval of 100–340 K.

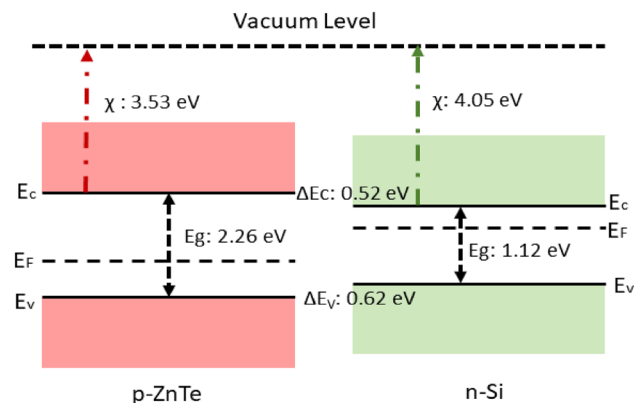


Fig. 1 Energy band diagram of the ZnTe/Si diode structure

Temperature of the samples was monitored and controlled using LakeShore 331 temperature controller. At each temperature step, current–voltage measurements were carried out by Keithley 2400 sourcemeter. During these measurements, illumination was provided by a 12 W halogen lamp at various illumination intensities between 20 and 115 mW/cm² controlled by Keithley 220 programmable current source. In addition, the diode characteristics of ZnTe/Si structure were analyzed by *I*–*V* measurements under dark and room temperature conditions. It was carried out in a bias voltage range of ±2 V applied between In-metal front contact on ZnTe layer and Ag-metal back contact on Si wafer and corresponding current flow is measured with Keithley 2401 sourcemeter using a computer-controlled measurement setup.

3 Results and discussion

The structural characterization of sputtered ZnTe thin films was accomplished by XRD and AFM measurements. XRD diffraction of ZnTe thin films is presented in Fig. 2 in the diffraction angle range of 20–70°. Three sharp and intensive peaks around 25.50, 42.00, 49.95° and one weak peak around 67.10° were observed in the XRD pattern [25, 41]. When these peaks were examined from the Joint Committee on Powder Diffraction Standards (JCPDS) card, it was seen that diffraction peaks are well consistent with JCPDS No. 15-0746 introducing the crystalline structure of the ZnTe as cubic with the lattice constant of $a = 0.6103$ nm. Miller indices associated with peaks are also given in the figure. The peaks in the XRD plot are

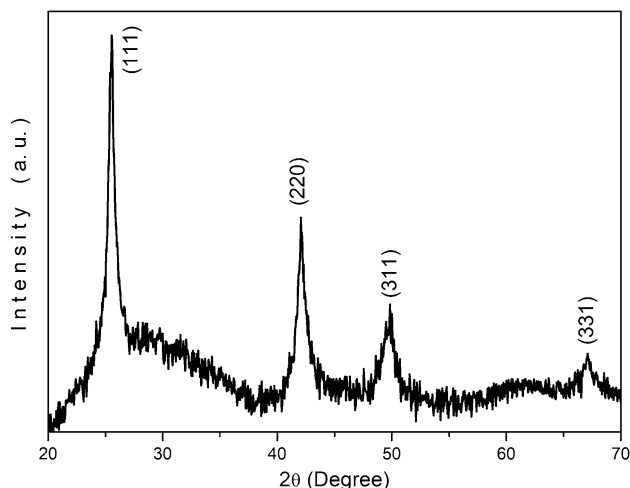


Fig. 2 XRD pattern of ZnTe thin films

utilized to get crystalline size (*D*) estimation taking into account the Debye–Scherrer’s relation given as [42],

$$D = 0.9\lambda/\beta \cos \theta \quad (1)$$

In Eq. 1, β and θ correspond to full-width at half maximum and diffraction angle, respectively. The usage of these parameters in Eq. 1 resulted in the crystalline size of ~14 nm. Williamson–Hall analysis was also applied to obtain strain (ϵ) of ZnTe thin films. Uniform deformation model is formulated as [43],

$$\beta \cos \theta = \frac{k\lambda}{D} + 4\epsilon \sin \theta \quad (2)$$

According to Eq. (2), $\beta \cos \theta$ vs. $4 \sin \theta$ plot gives a linear relation with a slope of ϵ and *y*-intercept of fitted line which corresponds to $k\lambda/D$. The ϵ and *D* values were estimated 1.8×10^{-3} and 12 nm, respectively [22].

The surface properties of the ZnTe films were investigated using AFM measurements performed in tapping mode. Three-dimensional AFM image of topography for $1 \mu\text{m} \times 1 \mu\text{m}$ area is given in Fig. 3a indicating the presence of a dense and smooth surface profile [44]. The roughness analysis on the two-dimensional AFM image (Fig. 3b) showed that the root-mean-square (RMS) surface roughness value was 1.08 nm. The phase image in Fig. 3c presents the resolution of the material phases and indicates the uniformity of the sample surface composition without any contamination and discontinuity.

Figure 4 shows Raman spectrum of sputtered thin films. Four Raman peaks around 126, 175, 204, and 406 cm⁻¹ were observed in the spectrum. The revealed mode frequencies in the spectrum are well correlated with those previously reported for ZnTe and Te in Refs. [45–47]. The Raman peak located around 126 cm⁻¹ is associated with A₁ mode of tellurium atom corresponding to chain expansion mode in which each atom moves in the basal plane [24]. The peaks around 175 and 204 cm⁻¹ were related to the fundamental transverse and longitudinal optical modes in ZnTe [45]. The weak Raman mode at 406 cm⁻¹ was attributed to the first overtone of the frequency of 204 cm⁻¹. The high-frequency dielectric constant (ϵ_∞) can be calculated from longitudinal (w_{LO}) and transverse (w_{TO}) frequencies using Lyddane–Sachs–Teller expression [48],

$$\left(\frac{w_{LO}}{w_{TO}} \right)^2 = \frac{\epsilon_0}{\epsilon_\infty} \quad (3)$$

where ϵ_0 symbolizes the static dielectric constant given as 10.4. The high-frequency dielectric constant of ZnTe thin films was calculated using Eq. 3 as 7.6 which is in good agreement with 7.3 reported in Ref. [46].

Fig. 3 **a** Three-dimensional AFM height, **b** two-dimensional AFM surface, and **c** two-dimensional AFM phase images of ZnTe thin films

The optical properties of these films were investigated by the room-temperature optical transmission measurements in the wavelength interval of 300–1000 nm, as shown in Fig. 5. In a general view of the presented spectrum, the active wavelength range can be presented as 500–1000 nm where the spectral transmittance dependency below 500 nm has a linear behavior with negligible value. As shown in this figure, the transmission spectrum has a higher transmission value with a maximum of 80% at higher wavelengths, on the other hand, there is a dominant absorption effect below 750 nm. The absorption coefficient, α , of the film layer was calculated using transmission values as,

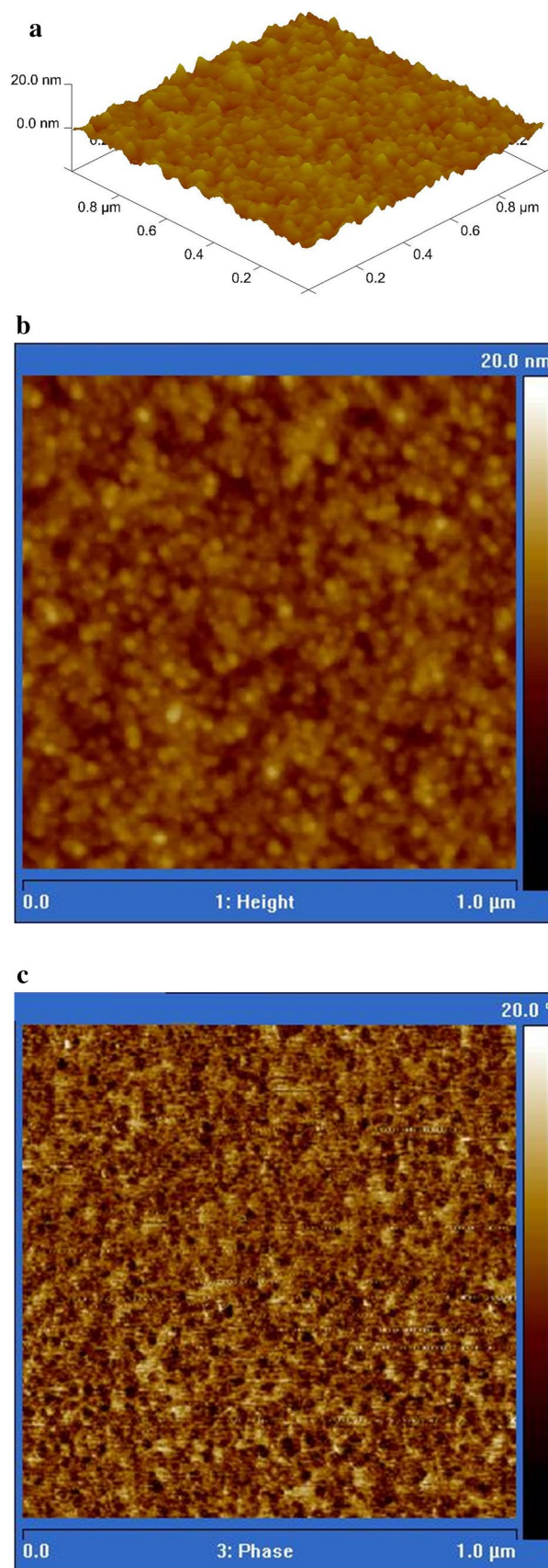
$$\alpha = \frac{1}{d} \ln\left(\frac{1}{T}\right) \quad (4)$$

where d is the film thickness and T is the normalized transmittance with respect to the uncoated glass substrate [49]. Using this relation, α values were calculated for each wavelength step and they were found about 10^{-4} cm^{-1} in the visible region. This average value can be related to the high-absorption characteristics. Based on these experimental results, band gap energy (E_g)–photon energy ($h\nu$) dependency was evaluated according to the direct optical transition model proposed by Tauc [49] as

$$\alpha h\nu = A(h\nu - E_g)^{1/2} \quad (5)$$

where A is a constant depending on optical transition probability. The obtained Tauc plot using Eq. 5 is presented as an inset of Fig. 5 and the room temperature E_g value of about 2.26 eV was obtained from the intersection point of linearly fitted line on the energy axis. Depending on the stoichiometry, it was found in a good agreement with previously reported values with different deposition methods [32, 40, 50].

The electrical measurements were performed on ZnTe thin films deposited in van der Pauw geometry and prepared with In front metal contact evaporation. The electrical properties were investigated by temperature-dependent current–voltage experiments under 5 V bias voltage in the 100–340 K range. The measured current values under constant bias were used to calculate conductivity (σ) of the sample according to the standard technique of four-contact van der Pauw method [51]. Room-temperature dark conductivity was obtained as $2.45 \times 10^{-4} (\Omega \text{ cm})^{-1}$ and in the interval of $2.47\text{--}2.65 \times 10^{-4} (\Omega \text{ cm})^{-1}$ with different illumination intensities. The temperature dependencies of dark σ values were plotted as given in Fig. 6. The experimental σ values were found in typical Arrhenius behavior. In the inset of this



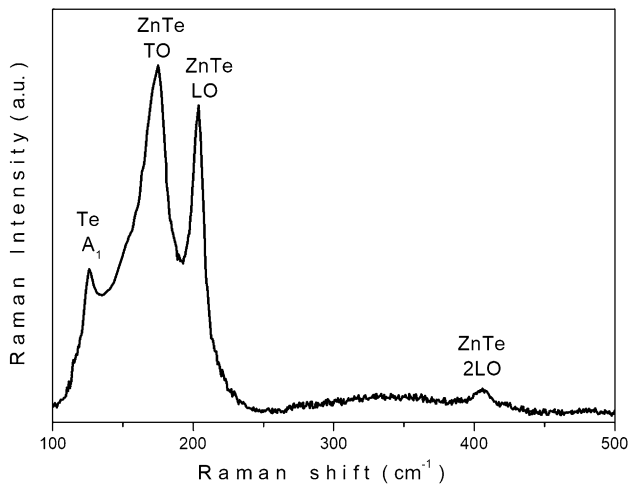


Fig. 4 Raman spectrum of ZnTe thin films

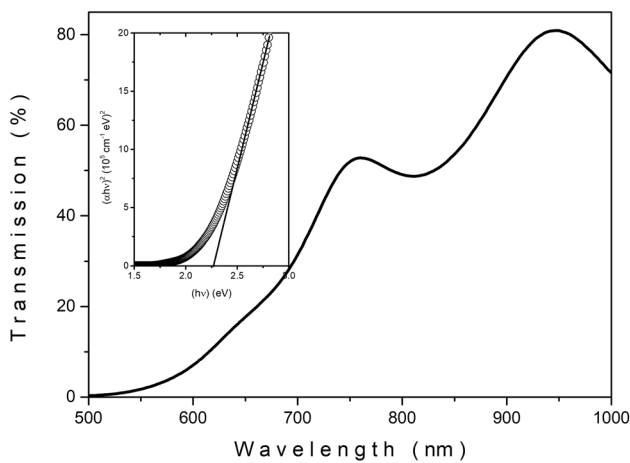


Fig. 5 Wavelength-dependent transmission values. (Inset shows the corresponding Tauc plot of ZnTe thin films)

figure, σ values were modeled according to the thermionic emission over the grain boundary potential as,

$$\sigma\sqrt{T} = \sigma_0 \exp\left(-\frac{E_a}{kT}\right) \quad (6)$$

where σ_0 and E_a are the parameters indicating pre-exponential factor and activation energy, respectively [52, 53]. In this analysis, the polycrystalline nature of the deposited ZnTe thin-film structure directs the analysis of electrical grain boundary behavior. Then, the variation of $\sigma\sqrt{T}$ with an inverse temperature is presented in Fig. 6 (inset) according to Eq. 6. The activation energy values were estimated by the relation of the $\ln(\sigma\sqrt{T})$ with $1/T$ and three linear regions with E_a values of 43, 20, and 7 meV were obtained in the temperature regions of 270–340, 170–260, and 100–160 K, respectively. These energy values can be associated with

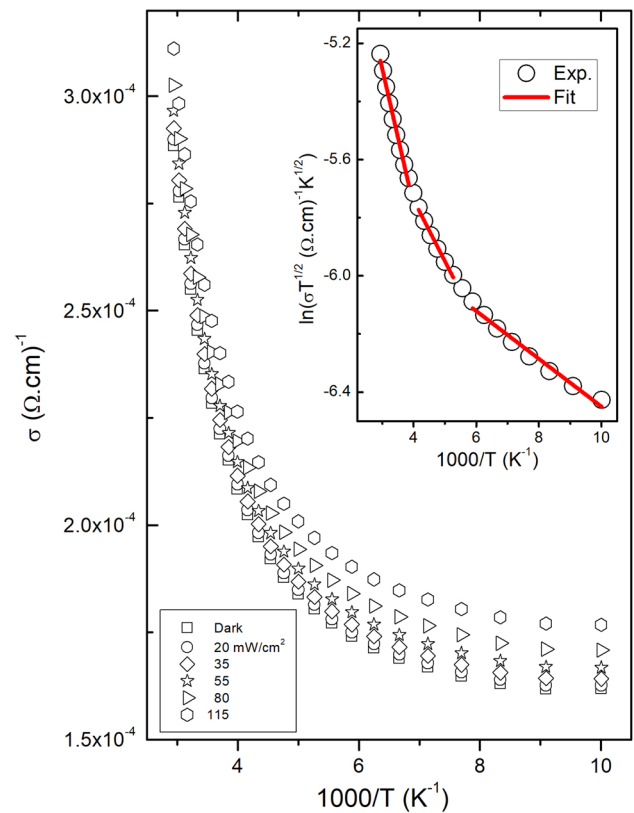


Fig. 6 The variation of conductivity with temperature and illumination intensity. Inset shows the analysis of activation energy using Eq. (4)

possible shallow trap centers due to the grain boundaries in the structure taking them into the conduction process [52–54].

The photoconductivity measurements of the samples placed about 0.5 cm below the lamp were carried out with different illumination intensities generated by a halogen lamp. As shown in Fig. 6, photoconductivity values were measured higher than those under dark conditions because of the contribution of excited carriers under illumination. This effect is shown in Fig. 7 as a variation in conductivity values with respect to the dark values ($\Delta\sigma = \sigma_{\text{photo}} - \sigma_{\text{dark}}$). As seen conductivity at a certain temperature increases with illumination intensity and contribution to the conductivity at a certain illumination intensity increases with increasing temperature. The photoconductivity contribution to the intrinsic conductivity can be directly related to the generation (or recombination) rate. Photocurrent (I_{pc}) and illumination intensity (Φ) can be associated with a power of an integer (m) which depends on the nature of recombination centers [55, 56]. Figure 8 presents the plots of $\ln(I_{pc})$ vs. $\ln(\Phi)$ at each temperature step, and it was found that the relation between I_{pc} and Φ follows the expression, $I_{pc} \propto \Phi^m$ with m between 1.28 and 1.48. This result can be associated

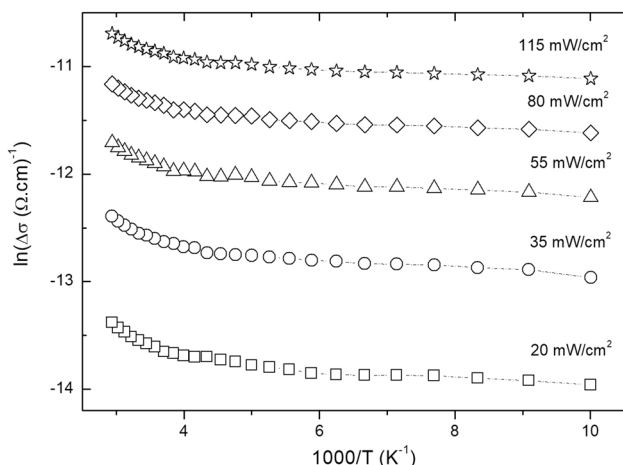


Fig. 7 The change in conductivity values ($\Delta\sigma$) at various temperatures and illumination intensities

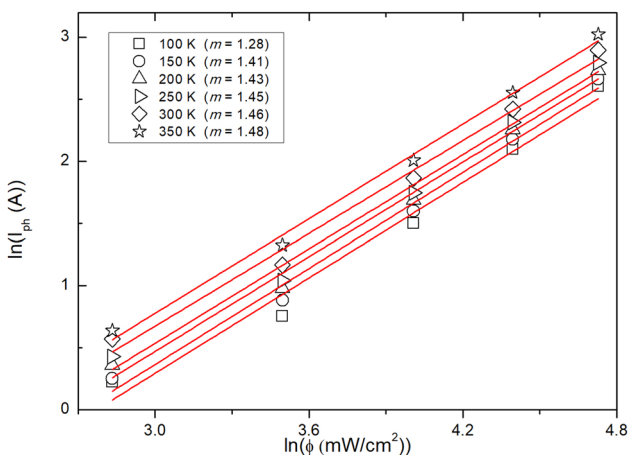


Fig. 8 The relation between photocurrent and illumination intensity at different temperatures

with the dominant effect of supralinear characteristics in the two-center recombination model [49]. In addition, an increase in photocurrent with temperature verifies the long life-time of free carriers and stronger recombination processes at the film surface.

In addition to the investigation of the material characteristics of ZnTe thin-film layer on glass, the deposition was performed on n-Si wafer substrate in order to evaluate its electrical response in a diode. This sample is used to investigate main diode parameters of the junction with well-known Si. In order to observe diode behavior of this Si-based heterostructure, room-temperature I – V measurement was carried out in the bias voltage limit of 2 V. As shown in Fig. 9, a rectifying behavior between these two semiconductor layers is observed with a rectification of about five-order in magnitude. From these data, zero-biased potential barrier (Φ_{b0}),

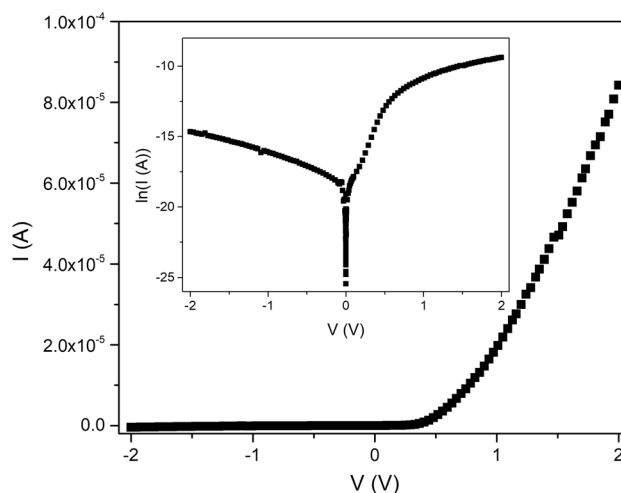


Fig. 9 I – V characteristics of ZnTe/Si diode structure (inset shows the logarithmic plot of I – V relation)

ideality factor (n), and series and shunt resistance (R_s and R_{sh}) values are calculated as the electrical parameters for this diode application. According to the exponential behavior at positive bias region in Fig. 9, forward current (I) flow through the diode is modeled according to thermionic emission (TE) theory given as,

$$I = I_0 \left[\exp\left(\frac{qV - IR_s}{nkT}\right) - 1 \right] \tag{7}$$

where the current values are measured with respect to the applied bias voltage (V) and the constants in this equation are q , k , n , and T as being an electronic charge, the Boltzmann constant, diode ideality factor, and the ambient temperature [38]. On the other hand, I_0 is the reverse saturation current in the relation with Φ_{b0} as,

$$I_0 = AA^*T^2 \left[\exp\left(-\frac{q\Phi_{b0}}{kT}\right) \right] \tag{8}$$

where A is the active diode area limited in the diameter of the dot-metal contact on ZnTe film layer (1 mm), A^* is the Richardson constant used in the value of 120 A/(cm² K²) for n-Si [38, 57]. Depending on possible non-ideal diode behavior under electrical potential, n is used to discuss the ideality of the fabricated diode where it can be derived from the linear relation between $\ln(I)$ and V as,

$$n = \frac{kT}{q} \left(\frac{d[\ln(I)]}{dV} \right) \tag{9}$$

Using Eq. 9, linear region in the $\ln(I)$ and V shown in the inset of Fig. 9 is modeled in a linear functional analysis by taking into consideration of $V > 3kT/q$ condition in order to eliminate the possible effects of parasitic resistances [38].

Therefore, from this linearity in the forward bias region, I_0 and n values were found as 5.16×10^{-8} A and 3.42 based on the intercept and slope of the obtained straight-line function. Equation 8 gives the relation between I_0 and Φ_{b0} where the other parameters constant, and thus Φ_{b0} was calculated as about 0.73 eV. These results are in good agreement with the works reported for different deposition techniques. Φ_{b0} and n values were reported as 0.68 eV and 2.63 for this heterojunction fabricated by thermal evaporated film layers, respectively [39]. On the other hand, there is a weak correlation between the results of this current work and the ones presented for vacuum-deposited ZnTe/Si diode where Φ_{b0} and n values were 1.93 and 0.28 eV [58]. The obtained n value is also higher than the value of electron-beam evaporated ZnTe/Si diode where it was reported as about 1.86 [32]. According to these results, the observed non-ideal behavior is a common result with literature, however, the deviation from ideality in the ZnTe/Si junction is more than these literature works and it can be attributed to the existence of unintended interfacial layer between the semiconducting layers, high rate of recombination at the depletion region and high parasitic resistances [39, 58]. Although the leakage current is in the range of the results of the similar works, the deviation from ideality is greater than previously reported values [39, 50, 58]. This fact can be related to the inhomogeneous barrier height formation with barrier patches around the mean barrier [7, 39]. In addition to the possible effects of parasitic resistance, interface between these semiconducting layers can be found in an active role to reconstruct the barrier to charge flow where it can be attributed to the possible recombination of the carriers at the interface trap [39, 59]. Together with these parameters, the parasitic resistances are the possible factors in the current flow through the diode. Their dominant effects are observed in the high forward and reverse bias regions, as shown in Fig. 9. These saturation characteristics in current values are used to derive the series (R_s) and shunt (R_{sh}) resistances at forward and reverse voltage regions, respectively. According to the Ohm's law, in general, these parasitic resistances can be defined as a ratio of current and voltage values in the form of $\partial V / \partial I$ [38, 60]. In this model, the deviations of the voltage ΔV depending on the parasitic resistance effects at a certain current data can be evaluated by the inverse slope of these voltage regions. As in the non-ideal diode characteristics, IR_s term is mainly used to describe the parasitic voltage drop due to the internal effects in Eq. 7 and also R_{sh} indicates the leakage current due the metal contacts and the surface inhomogeneities [38, 60]. Their effects are in the dominant role for the diode performance, and they are in comparable values with the similar diode applications, from the forward and reverse saturated regions, R_s and R_{sh} values were found as 780 and $4.7 \times 10^4 \Omega$, respectively [50]. Depending on the deposition method and applied depositional parameters

together with material characteristics of the deposited ZnTe thin film, these values are higher than the reported values, where they are 300 and 1420 Ω , for p-ZnTe/n-Si heterojunctions deposited by vacuum evaporation [58].

4 Conclusion

Material characteristics of ZnTe thin-film layer deposited by magnetron sputtering technique on glass substrate and its device properties on Si wafer substrate were investigated in the present study. Structural characterization methods showed that sputtered films are in a cubic crystalline lattice. These samples were found to be free from any pinholes and voids as observed from the surface scan using AFM and having an average surface roughness value around 1.08 nm. Furthermore, Raman spectrum presented four vibrational modes around 126, 175, 204, and 406 cm^{-1} and these results were well consistent with vibrational characteristics of ZnTe and Te, these modes verified the presence of the ZnTe phase in the film structure. Optical transmission measurements around a strong absorption below 750nm indicated its direct band gap characteristic. As a result, from conventional Tauc plot, E_g value was obtained as 2.26 eV. The temperature-dependent dark and photoconductivity values showed an exponential increase with temperature. According to the thermionic emission model, activation energy values were calculated as 7.0, 20.0, and 43.0 meV from the linear regions in the conductivity-temperature dependency. It was deduced that the power dependence of photocurrent with illumination intensity was related to the two-center recombination model and m values greater than unity indicate supralinear photoconductivity in the structure. In the structure of ZnTe/n-Si, a non-ideal diode behavior was observed with the value of 0.73 eV barrier height and the deviation from TE model was evaluated with the ideality factor as 3.42. The deviation from the ideality was associated with the possible surface inhomogeneity and trap states active in recombination. In addition, diode performance was evaluated with the R_s and R_{sh} values determined as about 7.8×10^2 and $4.7 \times 10^4 \Omega$, respectively. These results with polycrystalline structure, low surface roughness, and high band gap characteristics, deposited ZnTe film layer can be adopted to various device application. Reducing R_s of this heterostructure to a moderate level and improving interface of ZnTe/Si would end up with more promising practical results in technology.

References

1. S. Adachi, *Properties of Group-IV, III-V and II-VI Semiconductors* (Wiley, Hoboken, 2005)
2. M. Afzaal, P. O'Brien, J. Mater. Chem. **16**, 1597 (2006)
3. S.Z. Werta, O.K. Echendu, K.O. Egbo, F.B. Dejene, Thin Solid Films **689**, 137511 (2019)
4. I.M. Dharmadasa, A.A. Ojo, J. Mater. Sci. **28**, 16598 (2017)

5. G. Surucu, H.H. Gullu, O. Bayrakli, M. Parlak, *Polytech.* **20**, 801 (2017)
6. S.Z. Chen, R.S. Yu, L.G. Song, R.G. Zhang, X.Z. Cao, B.Y. Wang, P. Zhang, *Appl. Surf. Sci.* **498**, 143876 (2019)
7. H.H. Gullu, O. Bayrakli, D.E. Yildiz, M. Parlak, *J. Mater. Sci.* **28**, 17806 (2017)
8. M. Hazra, J. Datta, A.C.S. Appl. Mater. Interfaces **11**, 40393 (2019)
9. T. Chen, X. Wang, P. Han, W. Sun, S. Feng, J. Ye, Y. Xu, Y. Zhang, *J. Phys. D* **52**, 455101 (2019)
10. S. Giraldo, Z. Jehl, M. Placidi, V. Izquierdo-Roca, A. Perez-Rodriguez, E. Saucedo, *Adv. Mater.* **31**, 1806692 (2019)
11. K. Shen, X.Q. Wang, Y. Zhang, H.B. Zhu, Z.C. Chen, C.Z. Huang, Y.H. Mai, *Sol. Energy* **201**, 55 (2020)
12. M.A. Green, E.D. Dunlop, J. Hohl-Ebinger, M. Yoshita, N. Kopidakis, A.W.Y. Ho-Baillie, *Prog. Photovolt. Res. Appl.* **28**, 3 (2020)
13. N. Pandey, B. Kumar, D.K. Dwivedi, *Mater. Res. Exp.* **6**, 096425 (2019)
14. H.H. Gullu, *Optik* **178**, 45 (2019)
15. G. Ding, M. Wei, G. Surucu, Z. Liang, X. Wang, *Appl. Surf. Sci.* **491**, 750 (2019)
16. G. Surucu, K. Colakoglu, E. Deligoz, Y. Ciftci, N. Korozlu, *J. Mater. Sci.* **46**, 1007 (2011)
17. G. Surucu, K. Colakoglu, E. Deligoz, N. Korozlu, Y.O. Ciftci, *Solid State Commun.* **150**, 1413 (2010)
18. M. Betelli, N.S. Amade, D. Calestani, B. Garavelli, P. Pozzi, D. Macera, L. Zanotti, C.A. Gonano, M.C. Veale, A. Zapettini, *Nucl. Instrum. Meth. A* **960**, 163663 (2020)
19. S. Chanda, D. Ghosh, B. Debnath, M. Debbarma, R. Bhattacharjee, S. Chattopadhyaya, *Optik* **201**, 163510 (2020)
20. D. Ghosh, S. Chanda, B. Debnath, M. Debbarma, R. Bhattacharjee, S. Chattopadhyaya, *Phys. B* **574**, 411669 (2019)
21. W. Khan, S. Azam, I. Ullah, M. Rani, A. Younus, M. Irfan, P. Czaja, I.V. Kityk, *Crystals* **9**, 247 (2019)
22. H. Singh, P. Singh, A. Thakur, T. Singh, J. Sharma, *Mater. Sci. Semicond. Process.* **75**, 276 (2018)
23. H. Singh, M. Singh, J. Singh, B.S. Bansod, T. Singh, A. Thakur, M.F. Wani, J. Sharma, *J. Mater. Sci.* **30**, 3504 (2019)
24. M. Chaik, S.B. Moumen, A. Agdad, C.M. SambaVall, H. El-Aakib, H. AitDads, A. Outzourhit, L. Essaleh, *Phys. B* **572**, 76 (2019)
25. K.M.U. Rehman, X. Liu, M. Riaz, Y. Yang, S. Feng, M.W. Khan, A. Ahmad, M. Shezad, Z. Wazir, Z. Ali, K.M. Batoo, S.F. Adil, M. Khan, E.H. Raslan, *Phys. B* **560**, 204 (2019)
26. S. Ma, K. Li, H. Xu, J. Zhu, H. Wu, A.C.S. Appl. Mater. Interfaces **11**, 39342 (2019)
27. B. Xiao, M. Zhu, B. Zhang, J. Dong, L. Ji, H. Yu, X. Sun, W. Jie, Y. Xu, *Opt. Mater. Express* **8**, 431 (2018)
28. U.N. Roy, G.S. Camarda, Y. Cui, R. Gul, A. Hossain, G. Yang, J. Zazvorka, V. Dedic, J. Franc, R.B. James, *Sci. Rep.* **9**, 1620 (2019)
29. M.G.S.B. Ahamed, V.S. Nagarethinam, A. Thayumanavan, K.R. Murali, C. Sanjeeviraja, M. Jayachandran, *J. Mater. Sci.* **21**, 1229 (2010)
30. M. Isik, H.H. Gullu, M. Parlak, N.M. Gasanly, *Phys. B* **582**, 411968 (2020)
31. M. Nishio, K. Saito, Y. Nakatsuru, T. Shono, Y. Matsuo, A. Tomota, T. Tanaka, Q.X. Guo, *J. Cryst. Growth* **468**, 666 (2017)
32. K. Qin, L. Li, J. Huang, K. Tang, X. Zhang, M. Cao, Y. Shen, L. Wang, *Surf. Coat. Tech.* **320**, 153 (2017)
33. S. Ulicna, P.J.M. Isherwood, P.M. Kaminski, J.M. Walls, J. Li, C.A. Wolden, *Vacuum* **139**, 159 (2017)
34. Z.T. Kang, C.J. Summers, H. Menkara, B.K. Wagner, R. Dust, Y. Diawara, G. Mednikova, T. Thorson, *Appl. Phys. Lett.* **88**, 111904 (2006)
35. L.X. Hung, P.N. Thang, H.V. Nong, N.H. Yen, V.D. Chinh, L.V. Vu, N.T.T. Hien, W.D. de Marcillac, P.N. Hong, N.T. Loan, C. Schwob, A. Maitre, N.Q. Liem, P. Benalloul, L. Coolen, P.T. Nga, *J. Electron. Mater.* **45**, 4425 (2016)
36. Y.L. Cao, Z.T. Liu, L.M. Chen, Y.B. Tang, L.B. Luo, J.S. Jie, W.J. Zhang, S.T. Lee, C.S. Lee, *Opt. Exp.* **19**, 6100 (2011)
37. S. Rowtu, L.D.V. Sangani, M.G. Krishna, *J. Mater. Electron. Mater. Sci.* **47**, 1620 (2018)
38. S.M. Sze, K.N. Kwok, *Physics of Semiconductor Devices* (Wiley, Hoboken, 2007)
39. G.K. Rao, K.V. Bangera, G.K. Shivarkumar, *Curr. Appl. Phys.* **13**, 298 (2013)
40. S. Luo, H. Shen, X. He, Y. Zhang, J. Li, D. Oron, H. Lin, *J. Mater. Chem. C* **4**, 4740 (2016)
41. A.M. Salem, T.M. Dahy, Y.A. El-Gendy, *Phys. B* **408**, 3027 (2008)
42. B.D. Cullity, S.R. Stock, *Elements of X-ray Diffraction* (Prentice Hall, New Jersey, 2001)
43. M. Birkholz, *Thin Film Analysis by X-ray Scattering* (Wiley, Weinheim, 2006)
44. S. Rajpal, S.R. Kumar, *Phys. B* **534**, 145 (2018)
45. J.C. Irwin, J. Lacombe, *J. Appl. Phys.* **41**, 1444 (1970)
46. E. Constable, R.A. Lewis, *J. Appl. Phys.* **112**, 063104 (2012)
47. Y. Du, G. Qiu, Y. Wang, M. Si, X. Xu, W. Wu, P.D. Ye, *Nano Lett.* **17**, 3965 (2017)
48. R.H. Lyddane, R.G. Sachs, E. Teller, *Phys. Rev.* **59**, 673 (1941)
49. R.H. Bube, *Photoelectronic Properties of Semiconductors* (Cambridge University Press, Cambridge, 1992)
50. F. Aksoy Akgul, G. Akgul, H.H. Gullu, H.E. Unalan, R. Turan, *Philos. Magn.* **11**, 1164 (2015)
51. L.J. van der Pauw, *Philips Tech. Rev.* **20**, 220 (1958)
52. E. Coskun, H.H. Gullu, M. Parlak, C. Ercelebi, *J. Low Temp. Phys.* **178**, 162 (2015)
53. J.Y.W. Seto, *J. Appl. Phys.* **46**, 5247 (1975)
54. N.F. Mott, E.A. Davis, *Electronic Processes in Non-Crystalline Materials* (Clarendon Press, Oxford, 1971)
55. N.V. Joshi, *Photoconductivity, Art, Science, and Technology* (Marcel Dekker Inc., New York, 1990)
56. H.H. Gullu, E. Coskun, M. Parlak, *Braz. J. Phys.* **44**, 719 (2014)
57. D.K. Schroder, *Semiconductor Material and Device Characterization* (Wiley, New York, 1998)
58. M.A.M. Seyam, H.T. El-Shair, G.F. Salem, *Eur. Phys. J. Appl. Phys.* **41**, 221 (2008)
59. M. Ozer, D.E. Yildiz, S. Altindal, M.M. Bulbul, *Solid State Electron.* **51**, 941 (2007)
60. M. Kaleli, M. Parlak, C. Ercelebi, *Semicond. Sci. Technol.* **26**, 105013 (2011)

Publisher's Note Springer Nature remains neutral with regard to jurisdictional claims in published maps and institutional affiliations.